coatings

Article

Carbon Nanocoils and Polyvinyl Alcohol Composite Films for Fiber-Optic Fabry–Perot Acoustic Sensors

Yanming Sun [1], Zhe Dong [2], Zhezhe Ding [2], Neng Wang [1], Lei Sun [1], Heming Wei [3,*] and Guo Ping Wang [1,*]

1 College of Electronics and Information Engineering, Shenzhen University, Shenzhen 518060, China
2 Institute of Microscale Optoelectronics, Shenzhen University, Shenzhen 518060, China
3 Key Laboratory of Specialty Fiber Optics and Optical Access Networks, School of Communication & Information Engineering, Shanghai University, Shanghai 200444, China
* Correspondence: hmwei@shu.edu.cn (H.W.); gpwang@szu.edu.cn (G.P.W.); Tel.: +86-21-66136336 (H.W.)

Abstract: Carbon nanocoils (CNCs) are widely used in functional devices due to their helical morphology, which can be utilized in the fabrication of functional materials with unique properties. In this study, CNCs/polyvinyl alcohol (PVA) composite films were prepared using an electrostatic spinning method and used to form a diaphragm for Fabry–Perot acoustic sensors. With the addition of CNCs, the fabricated composite film showed enhanced mechanical performance responding to acoustic wave pressure. Considering the optical and mechanical response, the content of CNCs was set as 0.14 wt.%; the highest acoustic wave pressure response of the sensor was 1.89 V/Pa at 16.2 kHz, which was relatively higher than that of devices with pure polymer films. Additionally, the sensor had a broadband frequency response from 2 to 10 kHz. The results indicate that the proposed composite film acoustic sensor is suitable for low-frequency acoustic sensing, which lays the foundation for the extended application of functional sensors based on CNCs.

Keywords: carbon nanocoils; polyvinyl alcohol; composite films; acoustic sensing; Fabry–Perot

check for updates

Citation: Sun, Y.; Dong, Z.; Ding, Z.; Wang, N.; Sun, L.; Wei, H.; Wang, G.P. Carbon Nanocoils and Polyvinyl Alcohol Composite Films for Fiber-Optic Fabry–Perot Acoustic Sensors. *Coatings* **2022**, *12*, 1599. https://doi.org/10.3390/coatings12101599

Academic Editor: María Dolores Fernández Ramos

Received: 1 September 2022
Accepted: 19 October 2022
Published: 21 October 2022

1. Introduction

Highly sensitive acoustic sensors play an important role in modern society, with applications ranging from structural health monitoring (SHM) to biomedical imaging. The traditional technique for acoustic wave sensing is based on electroacoustic sensors, which are mainly divided into capacitive, piezoelectric and piezoresistive types [1]. The basic principle for this type of sensor is based on a change in deformation or resistance of the membrane when it is used for sensing acoustic waves. Although the electronic-based sensor is highly sensitive to acoustic waves, it poses significant issues in fabrication, signal transmission and demodulation. As the resonant frequency goes to the megahertz range, fabrication becomes difficult and the receiver can be noisy, especially when the sensors are arrayed [2].

Compared with electronic-based sensors, optical sensors, especially fiber-optic sensors, are interesting for acoustic sensing due to their advantages of compact size, light weight, remote sensing, immunity to electromagnetic interference, etc. [1]. Many optical fiber acoustic sensors are proposed, which are mainly based on surface plasmon resonance (SPR) [3,4], fiber gratings [5–7], fiber interferometers [8–11], etc. Although SPR sensors show a broadband frequency response, their optical quality factor (Q-factor) is relatively low, which is related to sensitivity. Grating-based devices are important sensing elements for the detection of acoustic waves due to their flexible multiplexing capability. However, their high-frequency response is limited, as the grating length is typically several millimeters, which is much larger than the acoustic wavelength. Fiber interferometers, especially Fabry–Perot interferometers (FPIs), are widely used as they have higher optical Q-factor and advanced materials, which can be utilized for fabricating the cavity, providing higher sensitivity. Notably, the material and size of the diaphragm determines the performance of the device in acoustic (pressure) sensing. Different materials, such as metal [12,13], polymer [14,15] and silicon/silica [16,17] have been proposed for the fabrication of thin film/diaphragm for devices. To improve sensitivity, two-dimensional (2D) materials are typically utilized as the thickness of the diaphragm can be much thinner [18–20]. However, thickness is hard to control and thin film could be broken, as mechanical performance could be problematic. An alternative method is to fabricate the membrane using composite materials for various applications [21–23]. Recently, polymer composites with different carbon nanostructures have been studied for acoustic wave generation and detection [24–27]. Although these do not show an obvious effect on the flexibility of fabricated films, sensitivity is indeed improved. Compared with these carbon nanostructures, Hayashida et al. tested the mechanical properties of a single carbon nanocoil (CNC) growing on the edge of the glass plate. They found that stretching could achieve 200% of the length [23], which proved that CNC has superelasticity, which can improve the sensor's sensitivity and ensure the film's flexibility at the same time.

In this study, we proposed and fabricated a Fabry–Perot cavity fiber-optic acoustic sensor, with a diaphragm based on CNCs and polyvinyl alcohol (PVA) composite films, using the electrostatic spinning method. CNCs are often used as conductive fillers for flexible strain sensing materials due to their excellent structural, electrical, thermal, mechanical and chemical properties. PVA is an electrolyte with excellent adhesion, and doped PVA could improve the ductility and flexible integrity of self-assembled CNCs films. The fabricated device had a relatively high fringe contrast. The results show that the fabricated device had a broadband frequency response and relatively high sensitivity to low-frequency acoustic waves; the proposed device with CNC–PVA composite film could be used for low-frequency acoustic wave sensing.

2. Materials and Methods

The chemicals used in this research were PVA powder (poly (vinyl alcohol) 1788, alcoholysis degree: 87.0%~89.0% (mol/mol), Aladdin, Shanghai, China), deionized water (DI water), Fe $(NO_3)_3 \cdot 9H_2O$ (AR, Mol. wt: 404.00, HUSHI, Shanghai, China), $SnCl_4 \cdot 5H_2O$ (AR, 99.0%, Macklin, Shanghai, China) and DMF (AR, 99.5%, Macklin, Shanghai, China).

2.1. Fabrication of CNCs–PVA Composite Film

First, the PVA powder was added to DI water, and then the solution was heated to 20 °C to dissolve, stir and soak at 300 r/min for 1 h. When the PVA powder was fully absorbed, the solution was heated to 85 °C, then stirred and heated for 3 h to prepare a PVA solution with a concentration of 10%. Next, we synthesized many carbon nanocoils at 710 °C using Fe/Sn as a catalyst using CVD technology (GSL-5Z-LCD), which has the ability to produce helical structures on a large scale with high yields. After that, 30 mg carbon nanocoils were added to a 22 g PVA solution and stirred to prepare a PVA/CNCs spinning mixture, with a CNCs content of approximately 0.14 wt.%. An electrospinning machine (SS-2, Ucalery, Beijing, China) was used to prepare PVA/CNCs composite film. Parameters related to electrospinning were set as follows: the syringe needle was model 22G, the receiver was a common roller receiver pasted with release paper, a voltage of +5/−5 kV was applied to the needle and the receiver, and the needle was 10 cm from the receiver. The syringe's injection speed was set at 0.05 mm/min, the syringe platform's translation speed was set at 500 mm/min, and the chamber's temperature was set at 25 °C. After spinning for 2 h, a flexible composite film of PVA/CNCs with size 12 cm × 7 cm was prepared.

2.2. Diaphragm-Based Fabry–Perot Sensor

CNC–PVA composite film can be designed as the diaphragm for FP acoustic sensors, of which the sensing principle is based on the deformation of the diaphragm induced by acoustic waves. According to the mechanical vibration theory, the resonant frequency is related to the diameter and thickness of the diaphragm and the Young's modulus and Poisson's ratio of the material, which can be given as [28]:

$$f_n = \frac{\alpha h}{2\pi r^2}\left[\frac{E}{12\rho(1-\nu^2)}\right]^{1/2} \tag{1}$$

where α is a constant, which is 10.21 for the fundamental mode of the diaphragm. ν, E and ρ are the Poisson's ratio, the Young's modulus and the density of the materials, respectively. r and h are the radius and thickness of the diaphragm, respectively. Figure 1a shows the frequency versus the radius and thickness of the diaphragm. In this study, we selected a glass tube with a 1.5 mm inner radius for fabricating the FP cavity. As the thickness increased from 10 to 50 µm, the resonant frequency increased from a few hertz to dozens of kilohertz. To simplify fabrication, we choose film with a 20 µm thickness, which contributed to a resonant frequency at 16.2 kHz, where a wave pressure of 100 Pa was used and a maximal deformation larger than 50 µm was obtained, as shown in Figure 1b.

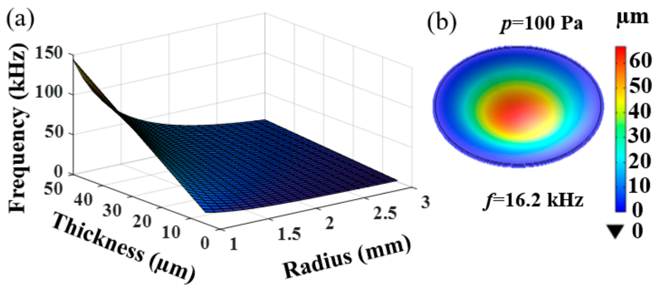

Figure 1. (**a**) Simulation of resonant frequency versus the thickness and radius of the diaphragm and (**b**) a resonant mode of the diaphragm at a frequency of 16.2 kHz.

The proposed device's schematics are shown in Figure 2. Figure 2a illustrates the model with a piece of optical fiber inserted into the silica tube. Light through the fiber was partly reflected from the fiber end facet/air interface and the air/diaphragm interface due to the Fresnel reflection, as shown in Figure 2b. The diaphragm's thin thickness and light absorption allowed the output interference signal to be described using two-beam interference, which can be given as [29]:

$$I \sim 2\sqrt{R_1 R_2}\cos\left(\frac{4\pi}{\lambda}n_0 L\right) \tag{2}$$

where I is the interference term of the output, the R_1 and R_2 are the reflectivity of the two reflected interfaces and $\varphi = 4\pi n_0 L/\lambda$ is the phase of the cavity. n_0 and L are the refractive index and the length of the cavity, respectively. As the sensor was used in the atmosphere environment, n_0 was approximately set as 1.

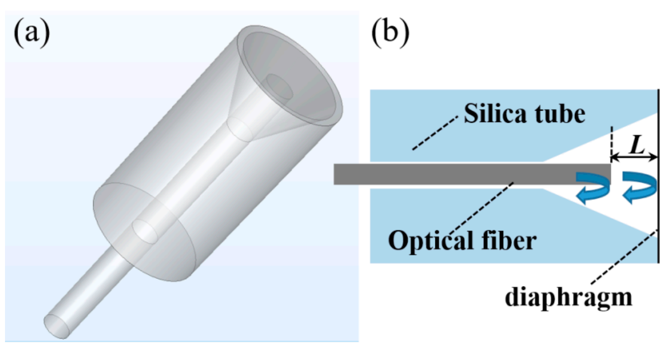

Figure 2. Schematic diagram of the proposed sensor: (**a**) side view of the Fabry–Perot cavity, and (**b**) model of the proposed sensor.

Notably, both optical and mechanical performances contribute to high sensitivity. The optical cavity length was carefully selected to optimize reflection from the diaphragm, thus, increasing the optical Q-factor. Additionally, considering the measurement range, the resonant frequency of the sensor was also investigated. For a clamped circular diaphragm, the displacement ($L(r_0)$) versus the applied pressure ($P(r_0)$) can be given as [30]:

$$L(r_0) = \frac{3(1-\nu^2)}{16Eh^3}\left(r^2 - {r_0}^2\right)^2 P(r_0) \tag{3}$$

where r_0 is the radial position from the central point of the diaphragm.

To analyse this deformation of the FPI further, the sensitivity can be illustrated as follows:

$$S = \frac{dI}{dP} = \frac{\partial I}{\partial \varphi} \times \frac{\partial \varphi}{\partial L} \times \frac{\partial L}{\partial P} \tag{4}$$

where the first term is related to the optical Q-factor of the interference fringe, the second term can be obtained from the phase equation in Equation (2), and the last term is related to the pressure, which is given by Equation (3).

2.3. Acoustic Wave Sensing

After fabricating the device, the acoustic sensing characterization of the CNCs–PVA-based FPI device was experimentally set up as shown in Figure 3a. In the test, a tunable laser was used as the source. Light was transmitted into a circulator (C) and then reflected by the FPI device. The reflected signal was detected by a photodetector (PD) and then acquired using a data acquisition (DAQ) card (NI-6211). A loudspeaker connecting a function generator (FG) was used to generate low-frequency acoustic waves. A standard microphone (GM1356) was used as a reference to characterize the generated acoustic wave pressure, which was close to the sound source. To obtain a maximal linear measuring range, the laser wavelength was tuned at the quadrature point, as shown in Figure 3b, which illustrates that a high sensitivity could be achieved when the Q factor was higher.

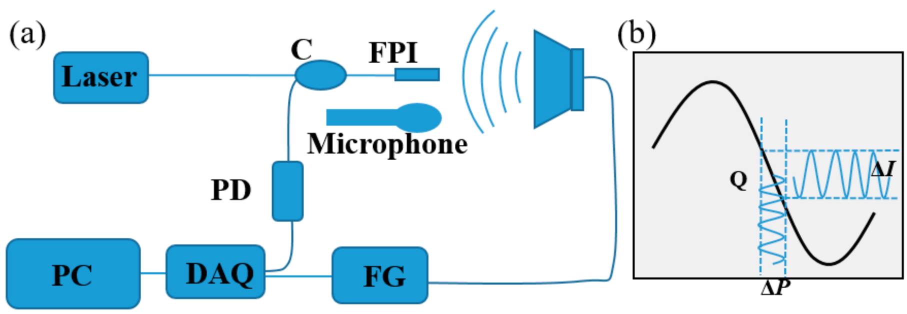

Figure 3. (**a**) Measuring setup for the detection of acoustic waves and (**b**) demodulation of the wavelength-locking method.

3. Results

3.1. Characterization of CNC–PVA Composite Film

Figure 4a shows a simple flow chart for the preparation of CNCs. CNCs were synthesized using a microwave heating method and CVD to realize large-scale production. CNCs' overall and partial morphology were observed via scanning electron image (SEM), as shown in Figure 4b,c. CNCs showed a unique geometric helical morphology. Figure 4d shows the CNCs' Raman shift, in which there were two main peaks, one peak at approximately 1322 cm^{-1} for D-band (which mainly originated from structural defects of the carbon material) and the other peak at approximately 1593 cm^{-1} for G-band (which originated from the graphite structure). A large D-band peak and a broad G-band peak in each spectrum indicated a low graphitization of CNCs. Transmission electron microscope (TEM) images of the CNCs displayed the details of helical architecture (Figure 4e). The fabricated

PVA/CNCs composite film was characterized. Figure 4f shows an optical photograph of the composited film, which clearly shows that the film was uniform; the film appears pale black due to the CNCs spun into the film during the electrostatic spinning process. Figure 4g shows the film's SEM; the interwoven CNCs and PVA fibers indicated that they could be well mixed by electrospinning, and also explained the film's uniformity, as shown in Figure 4f.

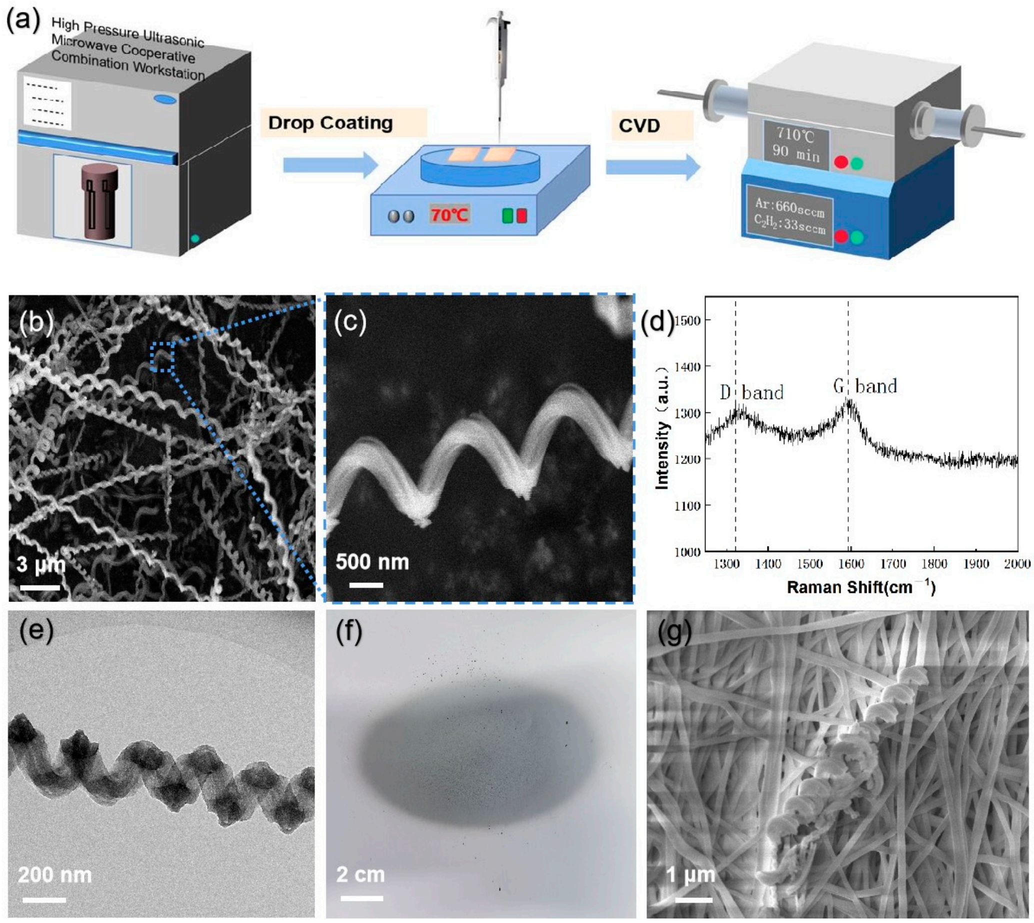

Figure 4. (**a**) Flow chart of CNCs preparation using the microwave heating method and CVD; (**b**) SEM image of CNCs; (**c**) SEM enlarged image of the partial CNC; (**d**) Raman shift of the CNCs; (**e**) TEM image of the partial CNC; (**f**) optical photograph of the fabricated composite film; and (**g**) SEM image of the fabricated film with CNCs.

3.2. Optical Response of the Fabricated Device

To characterize the fabricated device, a few films with different thicknesses were used to fabricate the device. First, we investigated the effect of thickness on the fringe contrast, and noted that the maximal fringe contrast could be obtained when the intensities of two reflected lights were the same. Figure 5a shows the measured fringe contrast versus the cavity length when the thickness of the diaphragm was 20 and 50 μm, separately. Thickness did not have an obvious effect on the reflection due to a large absorption of the material. The fringe contrast increased as the cavity length increased; however, it decreased as the length increased further. A maximal fringe contrast of 15 dB was obtained when the cavity length for the composite film was approximately 120 μm.

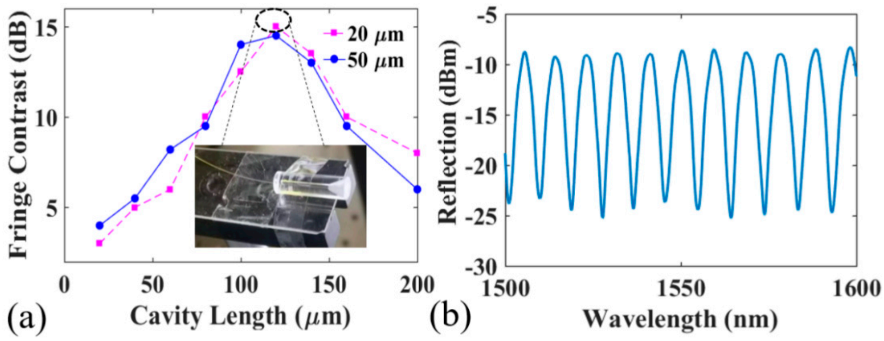

Figure 5. (**a**) The measured fringe contrast versus FP cavity with the composite diaphragm with different thicknesses and (**b**) measured reflection spectrum of the device of the inset showed in (**a**).

3.3. Performance Analysis of CNCs–PVA-Based FPI Acoustic Sensor

The fabricated FPI sensor was used for acoustic wave sensing. The experimental setup is shown in Figure 3. In the experiments, the FG generated voltage was kept constant to drive the speaker. The generated wave pressure at different frequencies was characterized. Figure 6 shows the demodulated time–domain signals detected by the proposed FPI acoustic sensor at frequencies of 500 Hz, 1 kHz, 4 kHz, 12 kHz and 16 kHz. Clearly, the sensor exhibited high sensitivities on the acoustic wave with different frequencies.

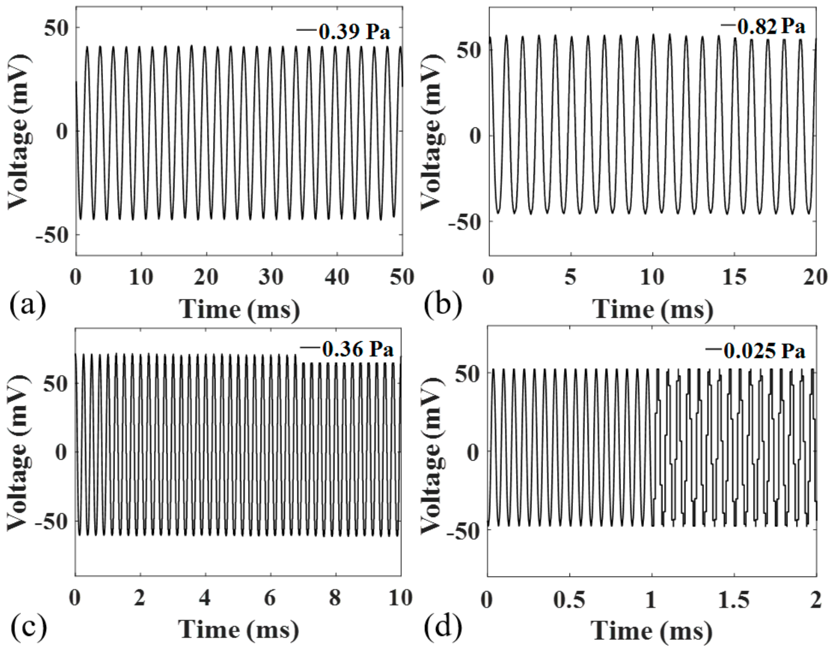

Figure 6. The measured time–domain response of the FPI sensor for the detection of acoustic waves with frequencies of (**a**) 500 Hz, (**b**) 1 kHz, (**c**) 4 kHz and (**d**) 16 kHz.

Next, as shown in Figure 7, the frequency spectra of the detected signals clearly indicated that only one frequency was obtained, as with the generated signal. To evaluate the frequency bandwidth, the input acoustic pressure was kept constant at 0.1 Pa and the frequency was swept from 100 Hz to 20 kHz. Figure 8 shows the sensor's frequency response, which had the largest amplitude at a frequency of 16.2 kHz, in accordance with the simulation. The sensitivity was evaluated as 1.89 V/Pa. However, the resonant frequency of the pure PVA polymer with a similar geometric size was approximatively located at 14 kHz. This difference had two primary causes: the difference in material properties, and improper fabrication, as the membranes' parameters could be slightly different. Notably, the mechanical response of a membrane did not obviously change, as the resonant frequency was slightly changed. To facilitate a direct comparison between the acoustic wave pressure responses of the two membranes, the optical Q-factors were the same, according to Equation (4). The sensitivity at the resonant frequency was evaluated as 1.35 V/Pa, which was lower than that of the device with the fabricated composite membrane. During the frequency range from 2 to 10 kHz, the frequency responses of the two sensors were relatively flat. It was noted that the resonant frequency of the sensor could be designed and tuned by changing the content of CNCs as well as the dimension of the diaphragm.

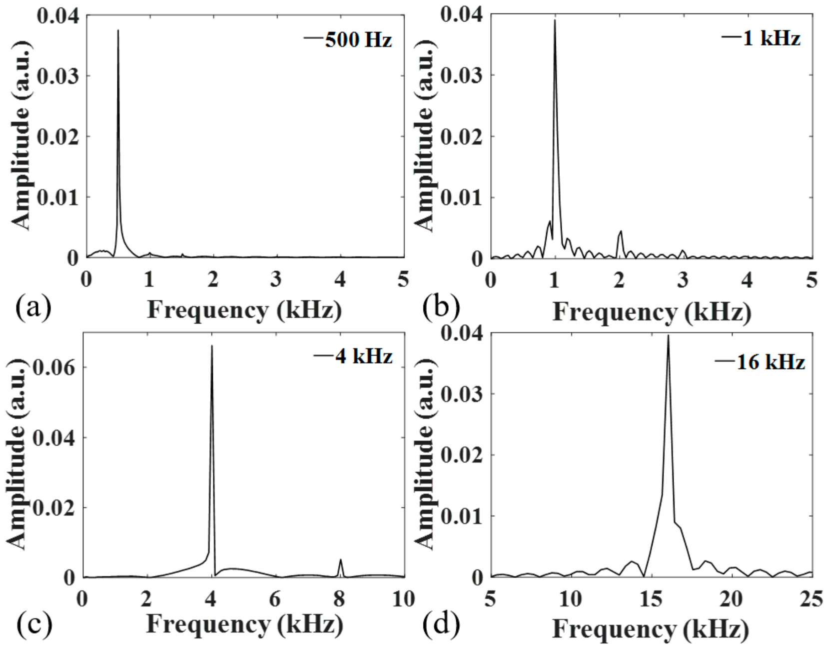

Figure 7. Frequency spectra of the detected signals with frequencies of (**a**) 500 Hz, (**b**) 1 kHz, (**c**) 4 kHz and (**d**) 16 kHz.

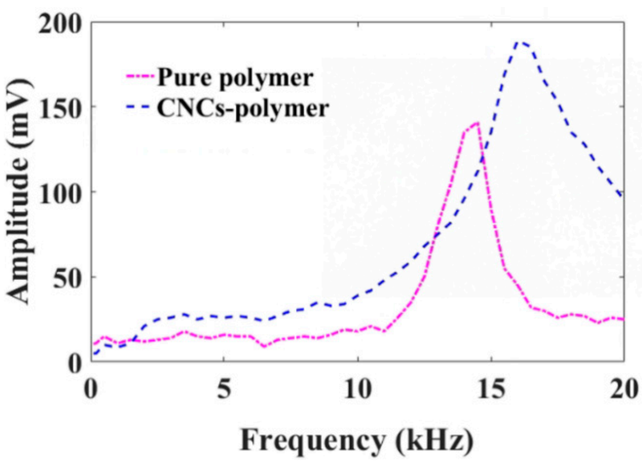

Figure 8. Frequency response of the fabricated FPI acoustic sensor.

To investigate sensor sensitivity at non-resonant frequencies further, two signals (at frequencies of 2 and 8.5 kHz) were applied. In the experiment, acoustic pressure increased from 5 to 100 mPa, and detected signals were obtained, as shown in Figure 9. A linear fitting was used. Amplitude versus pressure can be expressed as:

$$y_{2k} = 30.26P + 1.705, \quad R^2 = 0.9427 \tag{5}$$

$$y_{8.5k} = 36.57P - 0.4435, \quad R^2 = 0.9747 \tag{6}$$

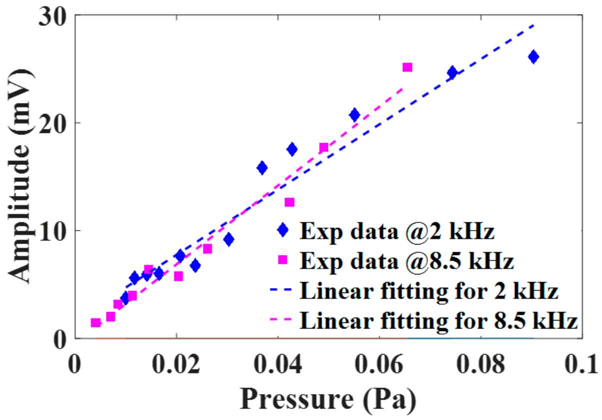

Figure 9. Acoustic frequency response of the fabricated sensor at 2 and 8.5 kHz.

The acoustic pressure sensitivity of the sensor at 2 and 8.5 kHz was estimated to be 302.6 and 365.7 mV/Pa, respectively, which was much higher than that of pure polymer-based acoustic sensors. In future, sensitivity can be further enhanced by optimizing the materials using CNCs' extensibility and flexibility. Additionally, the sensor's performance could have been affected by humidity, as the materials are highly sensitive to moisture [31,32]. Hence, resonant frequency could be shifted, which could be well-designed and utilized for highly sensitive humidity sensing [33,34] and triboelectric nanogenerators [35–37].

4. Conclusions

In this study, CNCs/polyvinyl alcohol (PVA) composite films were designed, fabricated and used in diaphragm-based Fabry–Perot acoustic sensors relying on diaphragm vibration. The enhanced mechanical performance of the composite film responding to acoustic wave pressure facilitated by the sensor's high acoustic sensitivity of 1.89 V/Pa at 16.2 kHz, which was relatively higher than devices with pure polymer films when the radius of the diaphragm was approximately 1.5 mm. The results demonstrated that the CNCs' composite membrane acoustic sensors were suitable for low-frequency acoustic sensing, which lays the foundation for extended applications of CNC-based functional sensors. However, the mechanical properties of CNC-based composited material has not yet been quantitatively characterized. Future studies will focus on mechanical analysis and material testing; then specific acoustic wave sensing performance can be achieved.

Author Contributions: Conceptualization, Y.S. and Z.D. (Zhe Dong); methodology, Y.S. and H.W.; software, Y.S.; validation, Y.S., Z.D. (Zhe Dong), Z.D. (Zhezhe Ding), N.W. and L.S.; formal analysis, Y.S., Z.D. (Zhe Dong) and H.W.; investigation, Y.S. and H.W.; resources, Y.S.; data curation, Y.S.; writing—original draft preparation, Y.S.; writing—review and editing, Y.S. and H.W.; visualization, Y.S.; supervision, G.P.W.; project administration, Y.S.; funding acquisition, Y.S. All authors have read and agreed to the published version of the manuscript.

Funding: This study was financially supported by the National Natural Science Foundation of China (Grant Nos. 62005153, 51908366, 11734012, 12074267 and 12174265), the Guangdong Natural Science Funds Grant (2021A1515012069), the Special Project for Research and Development in Key areas of Guangdong Province (2020B010190001) and the Guangdong Rural Science and Technology Commissioner Project (KTP20200226).

Institutional Review Board Statement: Not applicable.

Informed Consent Statement: Not applicable.

Data Availability Statement: Data that support the findings of this study are available from the corresponding author upon reasonable request.

Acknowledgments: The authors acknowledge assistance regarding HRTEM observation received from the Electron Microscope Center of Shenzhen University.

Conflicts of Interest: The authors declare no conflict of interest.

References

1. Chen, J.; Xue, C.; Zheng, Y.; Bai, J.; Zhao, X.; Wu, L.; Han, Y. Acoustic performance study of fiber-optic acoustic sensors based on fabry–pérot etalons with different q factors. *Micromachines* **2022**, *13*, 118. [CrossRef] [PubMed]
2. Chan, J.; Zheng, Z.; Bell, K.; Le, M.; Reza, P.H.; Yeow, J.T. Photoacoustic imaging with capacitive micromachined ultrasound transducers: Principles and developments. *Sensors* **2019**, *19*, 3617. [CrossRef] [PubMed]
3. Yang, T.; He, X.; Zhou, X.; Lei, Z.; Wang, Y.; Yang, J.; Cai, D.; Chen, S.-L.; Wang, X. Surface plasmon cavities on optical fiber end-facets for biomolecule and ultrasound detection. *Opt. Laser Technol.* **2018**, *101*, 468–478. [CrossRef]
4. Zhou, X.; Cai, D.; He, X.; Chen, S.-L.; Wang, X.; Yang, T. Ultrasound detection at fiber end-facets with surface plasmon resonance cavities. *Opt. Lett.* **2018**, *43*, 775–778. [CrossRef]
5. Qiao, Y.; Zhou, Y.; Krishnaswamy, S. Adaptive demodulation of dynamic signals from fiber Bragg gratings using two-wave mixing technology. *Appl. Opt.* **2006**, *45*, 5132–5142. [CrossRef]
6. Wei, H.; Tao, C.; Zhu, Y.; Krishnaswamy, S. Fiber Bragg grating dynamic strain sensor using an adaptive reflective semiconductor optical amplifier source. *Appl. Opt.* **2016**, *55*, 2752–2759. [CrossRef]
7. Yin, H.; Shao, Z.; Chen, F.; Qiao, X. Highly sensitive ultrasonic sensor based on polymer Bragg grating and its application for 3D imaging of seismic physical model. *J. Light. Technol.* **2022**, *40*, 5294–5299. [CrossRef]
8. Fomitchov, P.; Krishnaswamy, S.; Achenbach, J. Compact phase-shifted Sagnac interferometer for ultrasound detection. *Opt. Laser Technol.* **1997**, *29*, 333–338. [CrossRef]
9. Wei, H.; Krishnaswamy, S. Adaptive fiber-ring lasers based on an optical fiber Fabry–Perot cavity for high-frequency dynamic strain sensing. *Appl. Opt.* **2020**, *59*, 530–535. [CrossRef]
10. Wang, J.; Peng, H.; Zhou, P.; Guo, J.; Jia, B.; Wu, H. Sound source localization based on Michelson fiber optic interferometer array. *Opt. Fiber Technol.* **2019**, *51*, 112–117. [CrossRef]
11. Fan, P.; Yan, W.; Lu, P.; Zhang, W.; Zhang, W.; Fu, X.; Zhang, J. High sensitivity fiber-optic Michelson interferometric low-frequency acoustic sensor based on a gold diaphragm. *Opt. Express* **2020**, *28*, 25238–25249. [CrossRef] [PubMed]
12. Rong, Q.; Zhou, R.; Hao, Y.; Yin, X.; Shao, Z.; Gang, T.; Qiao, X. Ultrasonic sensitivity-improved Fabry–Perot interferometer using acoustic focusing and its application for noncontact imaging. *IEEE Photonics J.* **2017**, *9*, 6802511. [CrossRef]
13. Guo, F.; Fink, T.; Han, M.; Koester, L.; Turner, J.; Huang, J. Highsensitivity, high-frequency extrinsic Fabry-Perot interferometric fiber-tip sensor based on a thin silver diaphragm. *Opt. Lett.* **2012**, *37*, 1505–1507. [CrossRef] [PubMed]
14. Zhang, W.; Wang, R.; Rong, Q.; Qiao, X.; Guo, T.; Shao, Z.; Li, J.; Ma, W. An optical fiber Fabry-Perot interferometric sensor based on functionalized diaphragm for ultrasound detection and imaging. *IEEE Photonics J.* **2017**, *9*, 7103208. [CrossRef]
15. Wang, J.; Wang, M.; Xu, J.; Peng, L.; Yang, M.; Xia, M.; Jiang, D. Underwater blast wave pressure sensor based on polymer film fiber Fabry-Perot cavity. *Appl. Opt.* **2014**, *53*, 6494–6502. [CrossRef] [PubMed]
16. Guo, X.; Zhou, J.; Du, C.; Wang, X. Highly sensitive miniature all-silica fiber tip Fabry–Perot pressure sensor. *IEEE Photonics Technol. Lett.* **2019**, *31*, 689–692. [CrossRef]
17. Li, H.; Li, D.; Xiong, C.; Si, W.; Fu, C.; Yuan, P.; Yu, Y. Low-cost, high-performance fiber optic Fabry-Perot sensor for ultrasonic wave detection. *Sensors* **2019**, *19*, 406. [CrossRef]
18. Ma, J.; Jin, W.; Ho, H.L.; Dai, J.Y. High-sensitivity fiber-tip pressure sensor with graphene diaphragm. *Opt. Lett.* **2012**, *37*, 2493–2495. [CrossRef]
19. Yu, F.; Liu, Q.; Gan, X.; Hu, M.; Zhang, T.; Li, C.; Kang, F.; Terrones, M.; Lv, R. Ultrasensitive pressure detection of few-layer MoS_2. *Adv. Mater.* **2017**, *29*, 1603266. [CrossRef]
20. Wu, Y.; Yu, C.; Wu, F.; Li, C.; Zhou, J.; Gong, Y.; Rao, Y.; Chen, Y. A Highly sensitive Fiber-Optic microphone based on graphene oxide membrane. *J. Light. Technol.* **2017**, *35*, 4344–4349. [CrossRef]
21. Moradi, H.; Parvin, P.; Shahi, F.; Ojaghloo, A. Fiber optic Fabry-Pérot acoustic sensor using PVC and GO diaphragms. *OSA Contin.* **2020**, *3*, 943–951. [CrossRef]
22. Feng, Y.; Cai, R.; Zhou, Y.; Hu, Z.; Wang, Y.; Liu, D.; Han, S.; Zhao, J.; Xu, L.; Meng, Q. A high-performance porous flexible composite film sensor for tension monitoring. *RSC Adv.* **2022**, *12*, 26285–26296. [CrossRef]
23. Hayashida, T.; Pan, L.; Nakayama, Y. Mechanical and electrical properties of carbon tubule nanocoils. *Phys. B Condens. Matter* **2002**, *323*, 352–353. [CrossRef]
24. Yoo, G.; Yoon, H.; Heo, J.; Thakur, U.K.; Park, H.J.; Baac, H.W.; Heo, J. All-optical ultrasound transducer using CNT-PDMS and etalon thin-film structure. *IEEE Photonics J.* **2015**, *7*, 6803708. [CrossRef]
25. Baac, H.W.; Ok, J.G.; Park, H.J.; Ling, T.; Chen, S.-L.; Hart, A.J.; Guo, L.J. Carbon nanotube composite optoacoustic transmitters for strong and high frequency ultrasound generation. *Appl. Phys. Lett.* **2010**, *97*, 234104. [CrossRef]
26. Hsieh, B.-Y.; Kim, J.; Zhu, J.; Li, S.; Zhang, X.; Jiang, X. A laser ultrasound transducer using carbon nanofibers–polydimethylsiloxane composite thin film. *Appl. Phys. Lett.* **2015**, *106*, 021902. [CrossRef]

27. Biagi, E.; Margheri, F.; Menichelli, D. Efficient laser-ultrasound generation by using heavily absorbing films as targets. *IEEE Trans. Ultrason. Ferroelectr. Freq. Control.* **2001**, *48*, 1669–1680. [CrossRef]
28. Ma, J.; Xuan, H.; Ho, H.L.; Jin, W.; Yang, Y.; Fan, S. Fiber-optic Fabry–Pérot acoustic sensor with multilayer graphene diaphragm. *IEEE Photonics Technol. Lett.* **2013**, *25*, 932–935. [CrossRef]
29. Wei, H.; Chen, M.; Krishnaswamy, S. Three-dimensional-printed Fabry–Perot interferometer on an optical fiber tip for a gas pressure sensor. *Appl. Opt.* **2020**, *59*, 2173–2178. [CrossRef]
30. Yu, B.; Kim, D.W.; Deng, J.; Xiao, H.; Wang, A. Fiber Fabry-Perot sensors for detection of partial discharges in power transformers. *Appl. Opt.* **2003**, *42*, 3241–3250. [CrossRef]
31. Sun, Y.; Wang, C.; Pan, L.; Fu, X.; Yin, P.; Zou, H. Electrical conductivity of single polycrystalline-amorphous carbon nanocoils. *Carbon* **2016**, *98*, 285–290. [CrossRef]
32. Wu, J.; Sun, Y.-M.; Wu, Z.; Li, X.; Wang, N.; Tao, K.; Wang, G.P. Carbon nanocoil-based fast-response and flexible humidity sensor for multifunctional applications. *ACS Appl. Mater. Interfaces* **2019**, *11*, 4242–4251. [CrossRef] [PubMed]
33. Wang, Y.; Shen, C.; Lou, W.; Shentu, F. Fiber optic humidity sensor based on the graphene oxide/PVA composite film. *Opt. Commun.* **2016**, *372*, 229–234. [CrossRef]
34. Amin, E.M.; Karmakar, N.C.; Winther-Jensen, B. Polyvinyl-alcohol (PVA)-based RF humidity sensor in microwave frequency. *Prog. Electromagn. B* **2013**, *54*, 149–166. [CrossRef]
35. Wang, Y.; Zhang, L.; Lu, A. Highly stretchable, transparent cellulose/PVA composite hydrogel for multiple sensing and triboelectric nanogenerators. *J. Mater. Chem. A* **2020**, *8*, 13935–13941. [CrossRef]
36. Luo, X.; Zhu, L.; Wang, Y.; Li, J.; Nie, J.; Wang, Z.L. A flexible multifunctional triboelectric nanogenerator based on MXene/PVA hydrogel. *Adv. Funct. Mater.* **2021**, *31*, 2104928. [CrossRef]
37. Chen, X.; Yusuf, A.; del Rio, J.S.; Wang, D.-Y. A facile and robust route to polyvinyl alcohol-based triboelectric nanogenerator containing flame-retardant polyelectrolyte with improved output performance and fire safety. *Nano Energy* **2020**, *81*, 105656. [CrossRef]